RAPID MODELING OF HIGH RESOLUTION MOON-LIKE TERRAIN MODELS FOR TESTING OF OPTICAL LOCALIZATION METHODS

Martin Lingenauber[1], Tim Bodenmüller[1], Jan Bartelsen[2], Bolko Maass[3], Hans Krüger[3], Carsten Paproth[4], Sebastian Kuß[1], and Michael Suppa[1]

[1]*German Aerospace Center (DLR) - Institute of Robotics and Mechatronics - Departement of Perception and Cognition, Münchner Str. 20, 22334 Wessling, Germany, Email: firstname.lastname@dlr.de*

[2]*Bundeswehr University Munich - Institute of Applied Computer Science, Werner-Heisenberg-Weg 39, 85577 Neubiberg, Germany, Email: jan.bartelsen@unibw.de*

[3]*German Aerospace Center (DLR) - Institute of Space Systems - Department for Navigation and Control Systems, Robert-Hooke-Str. 7, 28359 Bremen, Germany, Email: firstname.lastname@dlr.de*

[4]*German Aerospace Center (DLR) - Institute of Robotics and Mechatronics - Department of Optical Information Systems, Rutherfordstr. 2, 12489 Berlin, Germany, Email: carsten.paproth@dlr.de*

ABSTRACT

This paper presents an intuitive approach for the rapid generation of arbitrary high resolution Digital Elevation Models (DEM) of moon-like surfaces, with minimal required extra expertise. It combines manual terrain shaping in a soil bin with automatic generation of 3 mm resolution DEMs. The generated DEMs are upscaled to 0.3 m resolution and integrated into lower-resolution DEMs of the lunar surface. The resulting model is used in the DLR project ATON (Autonomous Terrain based Optical Navigation) to realistically simulate optical sensors deployed on a lunar lander, enabling simulation of a complete landing trajectory until touch down. Results for five different landing site DEMs are provided to demonstrate the flexibility in modeling.

Key words: Testbed, Moon, Digital Elevation Model, Ground Truth Data.

1. INTRODUCTION

For future lander missions to the Moon, the German Aerospace Center (DLR) is investigating technologies for a navigation system that provides Autonomous Terrain based Optical Navigation (ATON). This shall allow precise landings on the lunar surface with an accuracy of 200 m 3 σ at a pre-defined landing site. A precise and robust position and attitude estimation of the lander during descent is achieved by the fusion of different sensors and estimation methods with a Kalman Filter. Data from Inertial Measurement Units (IMU) and a star tracker is combined with optical sensor data (camera, LIDAR). Different Computer Vision (CV) modules, such as feature tracking, crater navigation, and 3D matching, are integrated. The ATON system also contains an automatic terrain evaluation, which seeks out suitable spots of the landing area that allow a safe landing.

Within the ATON project the navigation system is tested in software simulation. For the simulation of optical sensors, a global Digital Elevation Model (DEM) of the lunar surface, the global ATON-DEM, was created from public databases. For latitudes between -60° and +60°, data products from the Kaguya Terrain Camera with a 3D resolution of about 10 m are used [1]. For the remaining polar regions, DEMs from the Lunar Reconnaissance Orbiter Laser Altimeter (LOLA) [2] are employed. In general, data sets with multiple resolutions are available [3] reaching from several hundred meters down to 5 m. A resolution of 100 m has been chosen to comply with criteria such as high coverage and non-abundance of artifacts. For altitudes higher than 20 km, this resolution proved to be sufficient for simulation purposes. However, below that altitude more detailed maps are required. In particular, the simulation of the final landing phase until touch down requires a resolution of 0.15 m, as an object of 0.5 m size should be represented by approx. 3 pixels to ensure a more robust obstacle detection. For some regions, non-global high resolution data sets are available. For example, a small part of the polar regions is provided at a 5 m resolution, based on LOLA data. Furthermore, several DEMs based on stereo pairs of the LRO Near Angle Camera (NAC) are available, providing a resolution of approx. 1 m [4]. However, all DEMs considered lacked artifact-free areas large enough.

Due to the discrepancy between the relevant properties of available DEM data and project requirements, e.g. 0.15 m resolution, low noise and nearly artifact free, high-resolution DEMs of possible landing sites and their surroundings were created in order to enhance the global ATON-DEM. Terrain shaping by hand in a soil bin is combined with an automatic generation of DEMs from camera images with the Semi-Global Matching algorithm [5] which was originally used for aerial imag-

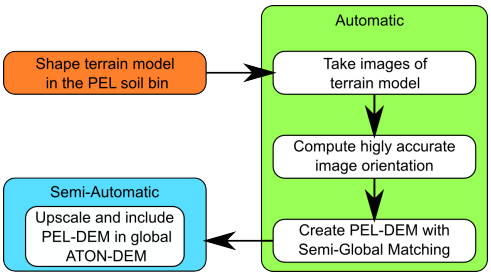

Figure 1: Overview of the rapid terrain modeling process

ing [6]. Finally, the generated DEMs are scaled by a factor of 100 and merged into the global ATON-DEM. The achieved resolution of the landing site is 0.3 m, more compliant to the project requirements than any other available data to date.

2. RELATED WORK

The problem of low resolution DEMs has been driving the development of several software applications aimed at artificially generating the missing detail. These include activities by the European Space Agency (ESA) developing the PANGU application [7], developments for the U.S. lunar landing research [8] and the China Lunar Exploration Project [9]. All approaches use low resolution DEMs or flat terrains as a starting point. This is followed by some form of fractal surface subdivision to add a representative roughness to the source material. Finally stones and craters are added, considering known lunar distribution functions as well as crater shape and decay models. Although the results of these programs are impressive, their availabilities are limited as they are subjected to restricted access. Furthermore, the softwares tend to require time consuming training.

The DLR Robotics and Mechatronics Institute (RM) Planetary Exploration Laboratory (PEL) (Fig. 2) is a testbed for planetary rover development [10], which allows to automatically generate high resolution DEMs of different terrains (more details in Sec. 3.1). Originally designed for the simulation of smaller areas, we applied it on a larger scale making use of the high resolution of the DEMs, which allows upscaling while maintaining a sufficient final resolution (see Sec. 3 and Sec. 4).

The software for the DEM generation is based on a stereo vision approach, namely the Semi-Global Matching (SGM) algorithm by [5]. Using a stereo vision system allows more dense DEMs compared to a laser scanning system due to reduced occlusions [10]. Additionally, the high quality of DEMs processed with the SGM has been proven in various applications [6].

Currently, there is no other test facility that combines the terrain shaping, the image recording and the DEM creation in such an easy to use, cost-, and time-efficient, manner as described in this paper.

3. METHODS

Following the overview of the rapid modeling process shown in Fig. 1, this sections explains in more detail the methods and tools used for it.

3.1. Planetary Exploration Laboratory

The DLR-RM PEL test facility consists of an indoor soil bin, a measurement system to generate DEMs and a pose tracking system [10] (Fig. 2). It is used to reproduce planetary surfaces for navigation tasks, to create high-resolution surface models and for planetary locomotion systems testing. The overall dimensions of the soil bin are $5\text{ m} \times 10\text{ m}$, and can be subdivided into multiple sections. For the terrain shaping, a section with a size of $6\text{ m} \times 5\text{ m}$ filled with gravel-sand was used.

The measurement system used to take images of a terrain model for the creation of DEMs, is attached to the ceiling above the soil bin (cf. Fig. 2). The hardware consists of a moveable beam, with five cameras attached, spanning the width of the bin. Due to its attachment to the two linear axes, the camera beam is moveable along the soil bin's long side and can be arbitrarily positioned. Hence, an image overlap of 80 % in the along track direction is possible whereas the cameras' Field Of View (FOV) overlap by 50 % in the across track direction. The measurement system is controlled by software to set up the cameras for automatic image acquisition, and to define the halting points of the camera beam. Once set up, it can automatically move the camera beam to the desired positions and record images of the soil bin. The possible precise positioning of the beam enables a fast computation of a low resolution DEM for preview purposes, although the image orientation is not as precise as required for high-resolution DEMs (cf. Sec. 3.3). This allows changes to the terrain model before launching the generation of the high quality DEM as described in Sec. 3.3. The intrinsic and extrinsic parameters of the single cameras and of the camera system are semi-automatically determined with the help of the DLR CalDe and the DLR CalLab software[1] (see [11] for details on calibration). In combination, this is an easy-to-use system that allows new users to be briefed within a day. It allows to concentrate on the shaping of the terrain models, because the DEM processing explained in Sec. 3.3 runs automatically.

3.2. Terrain Shaping in the PEL

The main purpose of the terrain shaping is to address the challenges a lunar surface poses to a visual navigation

[1] DLR CalDe and CalLab: http://www.robotic.dlr.de/callab, 2013

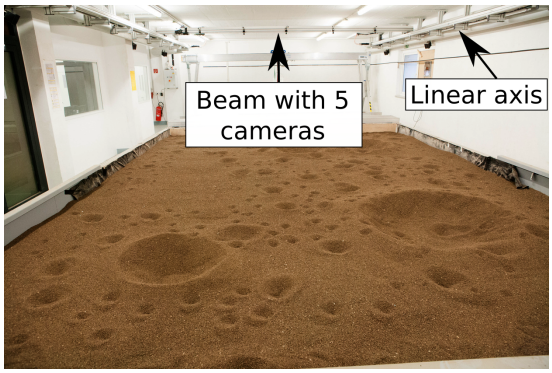

Figure 2: The DLR Planetary Exploration Laboratory with a 6×5 m terrain model, containing craters from small to large sizes. The measurement system with its five cameras on a movable beam system is used to record the terrain model.

system. As an engineering solution the resulting models may not be fully correct from a planetary science perspective.

Five terrain models with different characteristics were shaped (cf. Sec. 4), consisting of the following different landscape features. A smooth plane, as in model 1 (Fig. 7a) was the starting point for each model. By adding small hills and slopes or a high plateau (Fig. 7d and Fig. 7e), the topography of the models became more dynamic. To achieve a moon-like appearance of a model, it was covered with impact craters of different sizes. The various craters were distributed as randomly as possible, although no special random distribution was considered. Small craters (diameter 2 cm to 5 cm) and midsize craters (diameter 5 cm to 50 cm) were shaped by mimicking the impact of objects that lead to craters on the lunar surface. This was achieved by throwing stones of different size and with different amount of force on to the model for midsize craters. Thrusting a stick of approx. 2 cm diameter into the sand created smaller craters. Both impact techniques resulted in craters with a clearly visible rim as it was observed for the lunar surface [12, Sec. 4.1]. Larger craters, with a diameter of 50 cm to 1.5 m and mostly bowl shaped with a defined crater rim, were shaped by hand considering [12, Sec. 4.1]. The differently sized craters were combined to some extent, i.e. the wall and the rim of a larger crater might be covered by some smaller craters (e.g. as in Fig. 7c).

A steep ridge boundary of a high plateau (cf. Fig. 7d) was achieved by arranging stones next to each other. Sharply edged stones were used for this purpose, as this resulted in a more realistic appearance after the model's DEM was upscaled.

In order to mimic an existing lunar structure, a low resolution height map of an area can be used to model the topography (cf. Fig. 7f). The finer structures, which are usually not evident in such data sets, are added with the previously described techniques.

3.3. Automatic DEM Processing

The automatic processing of the camera data and the generation of a DEM can be divided into three steps: the *computation of camera orientations*, the pair wise *stereo matching*, and the *DEM generation* from the disparity images. The basic processing chain, although without an emphasis on the specific determination of the camera orientation as performed in this work, has already been described in [10]. The complete processing chain is briefly summarized below.

Computation of Camera Orientations
In order to provide the desired high accuracy, the stereo matching step requires the exact position and orientation of the five cameras at every point of acquisition. Initially, it was assumed that the mechanical stiffness of the measurement system would allow to use just one initial extrinsic calibration with the DLR CalLab software, i.e. only before the image capturing is launched (cf. [10]). Due to small unavoidable inaccuracies of the measurement system's linear axes, the resulting DEMs contained strong artifacts and the expected resolution could not be guaranteed. Particularly rotational perturbations that affect the camera orientation contributed to the observed artifacts. Whereas translational deviations were diminished by the FOV overlap in the along track direction.

Therefore, a more sophisticated approach by [13] was applied for the computation of the camera orientations. It computes the orientation for each camera position solely using information contained in the respective image set. Each of the five different image sets used for the DEMs presented in Sec. 4, was oriented in this way. The obtained precise relative orientations significantly reduced the previously observed artifacts, and increased the assured DEM resolution.

The approach of [13] is based on normalized cross correlation (NCC), least squares matching and robust bundle adjustment (see Fig. 3) and enables reliable results for point matching, even with less than ideal lighting conditions. Although the scene of the ATON image set is seemingly monotonously, a sufficient number of strong interest points can be extracted with the Förstner Operator [14]. Potential point-matches obtained by NCC are refined by least squares matching [15] using an affine geometric model. This results in relative sub-pixel point positions including covariance information. The points and their covariance information are employed for relative orientation of pairs and triplets. With the Five Point Algorithm [16] it is feasible to directly compute the relative orientation from calibrated image pairs. A version of it was embedded into RANdom SAmple Consensus - RANSAC [17] using the Geometric Robust Information Criterion - GRIC [18]. Additionally, a strategy similar to the Expectation Maximization (EM) algorithm is used to extend partial solutions. Triplets and associated calibrated trifocal tensors are the basic geometric building block of this approach. The triplets, in combination with least squares matching and robust bundle adjustment, are

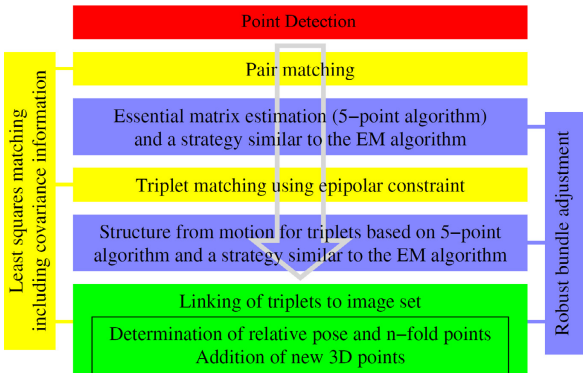

Figure 3: Image Orientation based on point matching, affine least squares matching and robust bundle adjustment.

used to propagate the complete relative orientation of an image set.

Stereo Matching
Stereo matching calculates a depth image from a pair of input images. The Semi-Global Matching (SGM) [5] was used, which has already been applied for the processing of aerial or satellite images [6]. The method uses Census to robustly match images with radiometric differences due to vignetting effects and different exposure times. The matching cost is combined with a smoothness cost that penalizes pixels that are associated to a different depth value than their neighbors. This is expressed in a global cost function that connects all pixels in the image with each other. Pixel-accurate matching is permitted by the formulation. Because finding a depth image that minimizes this cost function is known to be an NP problem, SGM optimizes it pathwise, symmetrically from eight directions through the whole image. As a result, the SGM method is very accurate at sharp depth discontinuities like object boundaries and maintains small features in the depth image.

The overlap across track is around 50% or less, depending on the height above ground, which is not enough for stereo matching. Therefore, the stereo matching for the set of PEL camera images is performed in the along track direction due to the large overlap of 80%. Each image is matched to the previous two and to the next two images.

Currently, the matching is performed in half of the full camera resolution due to the Bayer pattern of the used color cameras. Because SGM requires only monocolor images, the full resolution images are actually interpolated and slightly blurred. A matching of full resolution does not give better results.

DEM Creation
The result of the stereo matching is a set of depth images that correspond to the projection geometry of the input images. The DEM is created by reprojecting all depth images individually into an ortho projection and fusing the redundant depth information using a median [5]. This robustly removes remaining outliers. Holes due to mismatches are smoothly interpolated. Representative results are shown in Fig. 7.

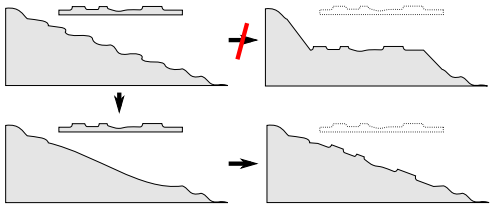

Figure 4: Correct blending procedure: From upper left to lower right, avoiding "shelving".

The resolution of the generated DEM is 3 mm, which corresponds to the Ground Sampling Distance (GSD) of the system. Because the intrinsic and the extrinsic calibration of the camera achieved with DLR CalLab and with the described computation of camera orientations is very accurate, the height error may be even half of the GSD, i.e. 1.5 mm, as the experience from aerial image processing has shown [19].

3.4. Upscaling and Inclusion in the Global ATON-DEM

Since the PEL-DEM is produced from a soil bin with a level foundation, it is difficult to realize large elevation dynamics without expending large quantities of material (sand) and/or loading the floor beyond the building's structural limits. A method is neccessary to blend the high-resolution, nearly level, PEL-DEM into the noisy and possibly sloped Kaguya DEM material. This process must preserve the useful high-resolution elevation dynamic within the PEL-DEM: locally discard the useless high-resolution noise content of the Kaguya DEM, while still preserving the large-scale sloping of the Kaguya elevation data to avoid creating a "shelf" for the landing site PEL-DEM (cf. Fig. 4). An anisotropic diffusion procedure was devised. It retains the large-scale dynamics (the slope) of the underlying Kaguya DEM everywhere, while gradually removing its high-frequency noise components from the center, where the PEL-DEM is to be merged, outwards. The idea stems from the established heat transfer equation

$$\frac{\partial}{\partial t}u(x,y,t) = \nabla \cdot (a(x,y)\nabla u(x,y,t)), \qquad (1)$$

where $u(x,y,t)$, in this context, can be understood to be the terrain elevation function of the underlying (x,y) plane at a specified moment t in the diffusion process, and $a(x,y)$ is a "heat conductivity map", which is constant in time, but not in space. "∇" is the gradient operator, whereas "$\nabla\cdot$" is the divergence operator. Omitting the arguments (x,y,t) and expanding the divergence, Eq. (1) can be simplified to

$$\frac{\partial}{\partial t}u = (\nabla a)^{\mathrm{T}}\nabla u + a\Delta u, \qquad (2)$$

with "Δ" denoting the Laplacien operator. This equation describes the transport of heat (or in our case, elevation) and conserves the total space integral over the function. But as this would simply transport the high-frequency content away from the area designated for merging the PEL-DEM it would result in an accumulation of very-high-frequency content around the landing site. Therefore an annealing term a^k was introduced into Eq. (2):

$$\frac{\partial}{\partial t}u = ((\nabla a)^{\mathrm{T}}\nabla u)\, a^k + a\Delta u. \tag{3}$$

The exponent k coarsely controls the amount of accumulated high-frequency content removed at the boundaries. As a partial differential equation on a uniformly-spaced grid (the DEM's support is a grid sampled at equidistant longitude-latitude points), Eq. (3) lends itself to a t-iteration and some finite-difference method for the differential operators. Starting the iterative process with the original Kaguya DEM $u(x, y, 0) := u(x, y)$, iterating as

$$u(x, y, i) = u(x, y, i-1) + \frac{\partial}{\partial t}u(x, y, i-1), \quad i = 1, \ldots, n \tag{4}$$

with $\frac{\partial}{\partial t}u(x, y, i-1)$ from Eq. (3), $u(x, y, n)$ (cf. Fig. 5h) is obtained. The final blended landing site DEM $w(x, y)$ is then obtained by combining the smoothed Kaguya DEM and the PEL-DEM additively as follows:

$$w(x, y) = u(x, y, n) + (v(x, y) - \overline{v(x, y)})v_{\text{mask}}(x, y), \tag{5}$$

where $\overline{v}$ denotes the mean of v and the border tapering mask v_{mask} (cf. Fig. 5d) is multiplied point-wise. The resulting $w(x, y)$ is shown in Fig. 5i. A simple implementation for this process is given here for MATLAB, using its Image Processing Toolbox[2]:

```
D2u = zeros(size(u));
Du = zeros(size(u , 1) , size(u , 2) , 2);
Da = cat(...
  3 , ...
  imfilter(a , -fspecial('sobel') , 'symmetric' , 'conv') , ...
  imfilter(a , -fspecial('sobel')' , 'symmetric' , 'conv') );
dtu = u;
tau = 1/4;
for t = 1:n
  D2u = imfilter(diff_u , fspecial('laplacian') , 'symmetric' , 'conv');
  Du = cat(...
    3 , ...
    imfilter(diff_u , -fspecial('sobel') , 0 , 'conv') , ...
    imfilter(diff_u , -fspecial('sobel')' , 0 , 'conv') );
  dtu = dtu + ...
    tau*((Da(:,:,1).*Du(:,:,1) + Da(:,:,2).*Du(:,:,2)).*a.^k + a.*D2u);
end
```

The above example uses "Du" as ∇u, "Da" as ∇a and "D2u" as Δu. By specifying an upper bound n for the number of iterations, one can control the strength of the smoothing. The factor "tau" guides numerical stability. This process is demonstrated in Fig. 5. Tweaking the relative sizes and scales of the PEL-DEM and the masks involved, one could obtain a nearly "gapless" transition from the underlying Kaguya DEM to the PEL-DEM, but only at the cost of the remaining Kaguya noise adding into the final landing site area.

The global ATON-DEM consists of tiles of approximately 2 km $\times$ 2 km size. After converting the upscaled PEL-DEM into a similar format as the original

[2]MATLAB version 7.13 and Image Processing Toolbox by The MathWorks Inc.: http://www.mathworks.com

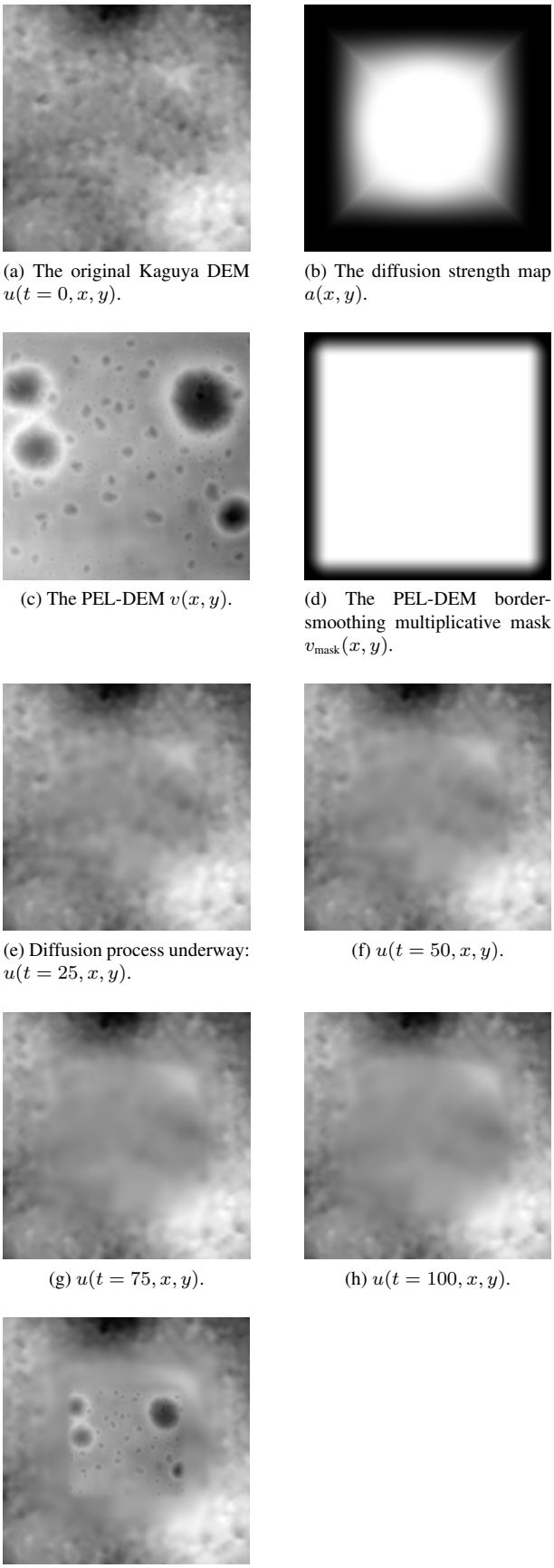

(a) The original Kaguya DEM $u(t = 0, x, y)$.

(b) The diffusion strength map $a(x, y)$.

(c) The PEL-DEM $v(x, y)$.

(d) The PEL-DEM border-smoothing multiplicative mask $v_{\text{mask}}(x, y)$.

(e) Diffusion process underway: $u(t = 25, x, y)$.

(f) $u(t = 50, x, y)$.

(g) $u(t = 75, x, y)$.

(h) $u(t = 100, x, y)$.

(i) The finished result $w(x, y)$.

Figure 5: The diffusion process for blending the variable-resolution PEL-DEM into the Kaguya DEM.

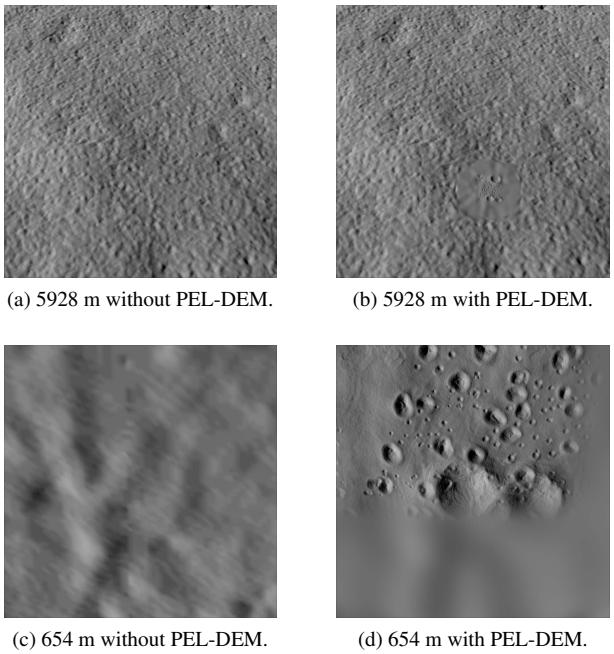

(a) 5928 m without PEL-DEM. (b) 5928 m with PEL-DEM.

(c) 654 m without PEL-DEM. (d) 654 m with PEL-DEM.

Figure 6: Results of the ATON camera simulation at two different altitudes, with and without the included high resolution DEM included.

moon DEM tiles and adding appropriate geographic coordinates, it could be easily included into the existing global ATON-DEM. Due to the chosen inclusion process, now two overlapping DEMs describe the same landing site, the low resolution Kaguya tile and the high resolution PEL-DEM tile. To create the required camera images for the testing of the ATON visual navigation system, the modular sensor simulation tool SENSOR++ [20] is used. For each point in time of the ATON descent simulation, the camera simulation module renders the global ATON-DEM with respect to the actual camera position. To avoid artifacts during the rendering, a prioritization mechanism was added to the ATON camera simulation, so that the high resolution landing site is preferably visible. As shown in Fig. 6, more details are visible after the inclusion of the PEL-DEM especially when approaching the landing site, although the blending procedure reduces the details around the high-resolution landing site.

4. RESULTS

A set of five terrain models, pictured in Fig. 7, was shaped in the PEL and processed to high resolution DEMs. Each terrain model was shaped to allow different test scenarios for the ATON optical navigation system. One to two landing sites are contained in each model. They are elliptical areas with no obstacles, none or only little slope and major axis lengths of 1 m to 2 m. After upscaling by a factor of 100, these areas enable testing the ATON project goal of a landing accuracy of 200 m 3 σ. The size of each PEL-DEM is approx. 6m $\times$ 5m, with two stripes of approx. 50 cm width on the top and bottom side of the models, required for the access to the models during the shaping process, i.e. the usable part of the PEL-DEMs is approx. 5m $\times$ 5m.

Model 1 (Fig. 7a), is a simple plane and can be used as a worst case test scenario for the visual navigation algorithms as no relevant features are detectable. *Model 2* (Fig. 7b) shows a variety of small to midsize craters and contains two landing sites close to each other (major axis length approx. 1 m). It is inteded for testing the visual navigation system's ability to cope with small suitable landing sites and with a high amount of craters.
Model 3 (Fig. 7c) shows four large craters shaped by hand. The only available landing site is on the right side (major axis length approx. 2 m). The purpose of the model is to determine the visual navigation system's ability to handle larger craters and the shadows casted by them.
Model 4 (Fig. 7d) represents a high plateau structure with a steep ridge boundary. One landing site (major axis length approx. 2 m) is on top of the plateau next to the large crater. The second site (major axis length approx. 1.5 m), is on the lower plane, close to the ridge. The model is designed for testing of the hazard avoidance while landing in proximity to ridge structures and to test how the visual navigation handles two available landing sites at different heights.
Model 5 (Fig. 7e) mimics an existing lunar structure located at the lunar south pole (latitude -89.4427°, longitude -137.3979°). It is a connecting ridge between two large craters as found at both lunar poles. Peaks of eternal light are located in such areas [21]. It was shaped considering the height map in Fig. 7f.

The resolution of the PEL-DEMs is approx. 3 mm. The bumps in the close-up view of model 3 in Fig. 7g are the result of clear rendering of small stones (2 cm to 5 cm size), which are added to the models in order to simulate boulders in the upscaled version.

All models are nearly free of artifacts that could have been caused by the DEM processing. Only in the areas where the FOVs of the five cameras overlap, are very thin edges evident, which are most strongly visible on the right side of each model (Fig. 7h), and nearly invisible in the middle part and on the left side. They are caused by small reprojection errors (approx. 0.5 pixels) which are below the calibration accuracy for the camera system. As this effect occurs at every image position, it becomes systematic, thus easily visible. Due to the edges' small size, no effects on the visual navigation algorithms were noticed during testing.

Model 3 was chosen as the most suitable for the specific mission scenario of ATON. After upscaling by a factor of 100, the resulting resolution was approx. 0.3 m. The result of the inclusion is shown in Fig. 6 by views taken at different altitudes during a simulated landing approach. In Fig. 6b, the difference in resolution between the lunar surface DEM, the smooth transition area and the high res-

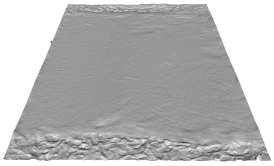

(a) Model 1 - Simple plane

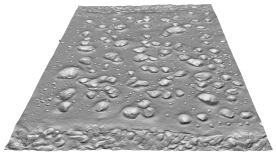

(b) Model 2 - Plane with multiple small to mid-size craters

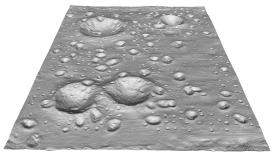

(c) Model 3 - Plane with small to large craters

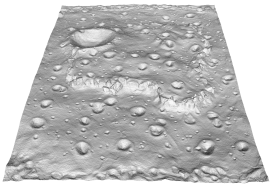

(d) Model 4 - High plateau in plane with small to large crater

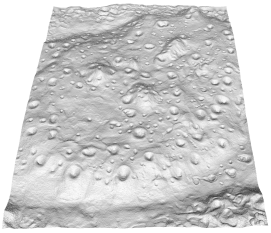

(e) Model 5 - Connecting ridge between two large craters

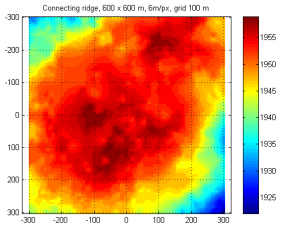

(f) Height map used as a guideline for model 4 (based on LRO LOLA data [3])

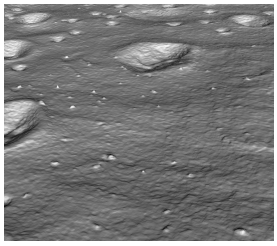

(g) Close-up of model 3 showing the resolution capability with stones of 2 cm to 5 cm size being visible as small bumps

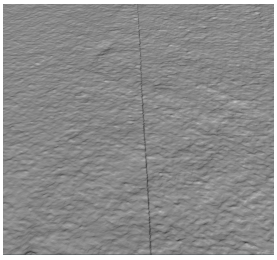

(h) Close-up of the right side of model 1 showing a thin edge – the only type of artifact visible in the models

Figure 7: The resulting set of DEMs create with the process described in section 3. The trampled down areas at the top and the bottom of the DEMs were used to access the terrain models during shaping and are neglected during the inclusion process.

olution DEM is clearly visible, while Fig. 6d shows the high level of detail available at low altitudes.

5. CONCLUSION AND OUTLOOK

Currently available DEMs of the lunar surface cannot be used directly to simulate lunar landings until touch down, due to their relatively low resolution. Enriching those DEMs with self-made high resolution DEMs of a landing site is shown in this paper. It is now possible to test and verify optical navigation methods for lunar landings.

The availability of current software solutions for DEM creation, e.g. PANGU [7], is often limited, and poses high demands of expertise and training of the user. In contrast, this paper demonstrates the possibility to quickly generate high resolution DEMs with a combination of terrain shaping and automatic DEM creation. As the terrain shaping is the only work required to be done by prospective users, this rapid modeling approch offers a less laborious way to achieve ground truth data for testing and simulation in planetary exploration projects.

Five different terrain models were shaped, each with a size of 5 m $\times$ 5 m, within only five days, with another week estimated for the processing and inclusion of all models. For the inclusion in the global ATON-DEM, the PEL-DEMs were upscaled by a factor of 100, resulting in a landing site DEM with a resolution of approx. 0.3 m, twice the initial requirement of 0.15 m, but still more than thirty times better than the 10 m resolution of the previously used Kaguya DEMs. Although the presented DEMs may not be fully correct from a planetary science point of view, they do show the topography required to test different technologies for planetary exploration. As they are intended to support technology development, quick production is another important advantage they provide.

In the future, a PEL-DEM resolution of 1 mm would be feasible, by using gray scale cameras instead of color cameras, by increasing the camera's chip resolution, or by increasing the focal length (requires more cameras) [10]. The correct modeling of shallow cavities or side parts of higher structures is in principle possible with the current measurement system. Instead of the 2.5-dimensional DEM, which allows only a single height value per grid element, a 3-dimensional data format is required.

Due to the high resolution of the produced DEMs and the flexibility of the terrain shaping, our approach may be suitable not only for lander missions, but also for the creation of data intended for testing long range rover navigation in different scenarios.

In the near future, it is planned to offer the usage of the PEL for rapid terrain modeling to interested research groups and organizations upon request.

ACKNOWLEDGMENTS

We want to thank Heiko Hirschmüller and Andreas Kuhn for their support with the PEL processing as well as Maximilian Apfelbeck for his support with operating the PEL. Our special thanks go to Mark Verveld and Daniel Lüdtke for their help on shaping the models.

REFERENCES

[1] J. Haruyama, S. Hara, K. Hioki, A. Iwasaki, T. Morota, M. Ohtake, T. Matsunaga, H. Araki, K. Matsumoto, Y. Ishihara, H. Noda, S. Sasaki, S. Goossens, and T. Iwata. Lunar Global Digital Terrain Model Dataset Produced from SELENE (Kaguya) Terrain Camera Stereo Observations. In *Lunar and Planetary Inst. Science Conf. Abstracts*, volume 43 of *Lunar and Planetary Inst. Tech. Report*, page 1200, The Woodlands, Texas, USA, March 2012.

[2] David M. H. Baker, James W. Head, Gregory A. Neumann, David E. Smith, and Maria T. Zuber. The transition from complex craters to multi-ring basins on the Moon: Quantitative geometric properties from Lunar Reconnaissance Orbiter Lunar Orbiter Laser Altimeter (LOLA) data. *J. Geophys. Res.: Planets*, 117(E12):1–29, 2012.

[3] PDS Geosciences Node. Lunar Orbital Data Explorer. `http://ode.rsl.wustl.edu/moon/`, 2013.

[4] T. Tran, M. Rosiek, E. Howington-Kraus, B. Archinal, E. Anderson, and LS Team. Generating digital terrain models using LROC NAC images. In *Geospatial Data and Geovisualization: Environment, Security, and Society - Special Joint Symp. of ISPRS Commission IV and AutoCarto 2010 in conjunction with ASPRS/CaGIS 2010 Special Conf.*, pages 15–19, 2010.

[5] H. Hirschmüller. Stereo Processing by Semiglobal Matching and Mutual Information. *IEEE Trans. Pattern Anal. Mach. Intell.*, 30(2):328–341, February 2008.

[6] H. Hirschmüller. Semi-Global Matching - Motivation, Developments and Applications. *Photogrammetric Week*, 11:173–184, 2011.

[7] Nick Rowell, Steve Parkes, Martin Dunstan, and Olivier Dubois-Matra. PANGU: Virtual spacecraft image generation. In *5th Int. Conf. on Astrodynamics Tools and Techniques, ICATT 2012*, ESA ESTEC, Noordwijk, The Netherlands, 2012.

[8] U.J. Shankar, Wen-Jong Shyong, T.B. Criss, and D. Adams. Lunar Terrain Surface Modeling for the ALHAT Program. In *2008 IEEE Aerospace Conf.*, pages 1–10, Big Sky, Montana, USA, 2008.

[9] Xianlin Huang, Xiaonan Jiang, Ting Yu, and Hang Yin. Fractal-Based Lunar Terrain Surface Modeling for the Soft Landing Navigation. In *2nd Int. Conf. on Intelligent Computation Technology and Automation, ICICTA 2009*, volume 2, pages 53–56, Changsha, Hunan, China, 2009.

[10] B. Rebele, A. Wedler, M. Apfelbeck, H. Hirschmüller, S. Kuss, A. Gibbesch B. Schäfer, and G. Hirzinger. Advanced Testbed and Simulation Environment for Planetary Exploration and Mobility Investigations. In *Proc. of the 10th Int. Symp. on Artificial Intelligence, Robotics and Automation in Space, i-SAIRAS 2010*, pages 330–337, Sapporo, Japan, 2010.

[11] K. H. Strobl and G. Hirzinger. More accurate camera and hand-eye calibrations with unknown grid pattern dimensions. In *2008 IEEE Int. Conf. on Robotics and Automation, ICRA 2008*, pages 1398–1405, Pasadena, California, USA, May 2008. IEEE.

[12] G.H. Heiken, D.T. Vaniman, and B.M. French, editors. *The Lunar Sourcebook: A User's Guide to the Moon*. Cambrige University Press, 1991.

[13] J. Bartelsen, H. Mayer, H. Hirschmüller, A. Kuhn, and M. Michelini. Orientation and Dense Reconstruction of Unordered Terrestrial and Aerial Wide Baseline Image Sets. *ISPRS Annals of Photogrammetry, Remote Sensing and Spatial Information Sciences*, I-3:25–30, 2012.

[14] W. Förstner and E. Gülch. A Fast Operator for Detection and Precise Location of Distinct Points, Corners and Centres of Circular Features. In *ISPRS Intercommission Conf. on Fast Processing of Photogrammetric Data*, pages 281–305, Zürich, Switzerland, 1987.

[15] A.W. Grün. Adaptive Least Squares Correlation: A Powerful Image Matching Technique. *South African J. of Photogrammetry, Remote Sensing and Cartography*, 14(3):175–187, 1985.

[16] D. Nistér. An efficient solution to the five-point relative pose problem. In *Proc. of the 2003 IEEE Computer Society Conf. on Computer Vision And Pattern Recognition, CVPR 2003*, volume 2, pages II–195–202 vol.2, Madison, Wisconsin, USA, 2003.

[17] M.A. Fischler and R.C. Bolles. Random Sample Consensus: A Paradigm for Model Fitting with Applications to Image Analysis and Automated Cartography. *Communications of the ACM*, 24(6):381–395, 1981.

[18] P.H.S. Torr and A. Zisserman. Robust Parametrization and Computation of the Trifocal Tensor. *Image and Vision Computing*, 15:591–605, 1997.

[19] H. Hirschmüller and T. Bucher. Evaluation of Digital Surface Models by Semi-Global Matching. In *DGPF 2010*, Vienna, Austria, 2010.

[20] C. Paproth, E. Schlüßler, P. Scherbaum, and A. Börner. SENSOR++: simulation of remote sensing systems from visible to thermal infrared. In *Int. Archives of the Photogrammetry, Remote Sensing and Spatial Information Sciences*, volume XXXIX-B1 of *XXII ISPRS Congress*, pages 257–260, Melbourne, Australia, 2012.

[21] M. Kruijff. Peaks of Eternal Light on the Lunar South Pole - How They Were Found and What They Look Like. In B. H.Foing and M. Perry, editors, *Proc. of the 4th Int. Conf. on Exploration and Utilisation of the Moon, ICEUM 4*, volume 462 of *ESA Special Publications*, pages 333–336, ESA ESTEC, Noordwijk, The Netherlands, September 2000. European Space Agency.